Electronic "photoreceptors" enable prosthetic vision with acuity matching the natural resolution in rats

Bing-Yi Wang[1,*], Zhijie Charles Chen[2,*], Mohajeet Bhuckory[3,4], Tiffany Huang[2], Andrew Shin[5], Valentina Zuckerman[3], Elton Ho[3,4], Ethan Rosenfeld[3], Ludwig Galambos[2], Theodore Kamins[2,3], Keith Mathieson[6], and Daniel Palanker[3,4]

[1] Department of Physics, Stanford University, Stanford, CA, USA
[2] Department of Electrical Engineering, Stanford University, Stanford, CA, USA
[3] Hansen Experimental Physics Laboratory, Stanford University, Stanford, CA, USA
[4] Department of Ophthalmology, Stanford University, Stanford, CA, USA
[5] Department of Material Science, Stanford University, Stanford, CA, USA
[6] Department of Physics, Institute of Photonics, University of Strathclyde, Glasgow, Scotland, UK
* These authors contributed equally to this work.

Abstract

Localized stimulation of the inner retinal neurons for high-acuity prosthetic vision requires small pixels and minimal cross-talk from neighboring electrodes. Local return electrodes within each pixel can limit the crosstalk, but they over-constrain the electric field, thus precluding the efficient stimulation with subretinal pixels smaller than 50 μm. Here we demonstrate a high-resolution prosthetic vision based on a novel design of a photovoltaic array, where field confinement is achieved dynamically, leveraging the adjustable conductivity of the diodes under forward bias to turn the designated pixels into transient returns. We validated computational modeling of the field confinement in such an optically-controlled circuit by ex-vivo and in-vivo measurements. Most importantly, we demonstrated that by using this strategy, the grating acuity of prosthetic vision with 20 μm pixels matches the 28 μm limit of the natural visual acuity in rats. This method will enable customized field shaping for each patient based on individual retinal thickness and distance from the implant, paving the way to prosthetic vision with acuity as high as 20/80 in atrophic macular degeneration.

Introduction

Retinal degenerative diseases, such as age-related macular degeneration (AMD) and retinitis pigmentosa, are a leading cause of untreatable visual impairment and legal blindness[1,2]. Despite the irreversible loss of photoreceptors, the inner retinal neurons survive to a large extent[3,4]. Electrical stimulation of the secondary retinal neurons, mainly the bipolar cells, elicits visual percepts[5,6], hence enabling electronic restoration of sight (Figure 1). AMD patients with a photovoltaic subretinal implant PRIMA (Pixium Vision, Paris, France) having bipolar pixels of 100 μm in width (corresponding to Snellen acuity of 20/420) demonstrated prosthetic letter acuity of 1.17 ± 0.13 pixels, corresponding to the Snellen range of 20/460–20/565[5]. Even though this is a very exciting proof of concept, for a wide adoption of this approach by AMD patients, prosthetic acuity should significantly exceed their remaining peripheral vision, which is typically no worse than 20/400. The sampling limit for acuity of 20/200 (US legal blindness threshold) corresponds to 50 μm pixels and of 20/100 – to 25 μm pixels.

As with natural vision, prosthetic visual acuity is fundamentally limited not only by the spatial resolution of the stimulation patterns (i.e. pixel size and the field spread), but also by their contrast, which is affected by crosstalk between the neighboring electrodes[7]. Lateral spread of electric field can be confined by the local return electrodes in each pixel, as in the PRIMA implant, but scaling down such pixels is difficult because penetration depth of electric field in tissue is constrained by the distance between the active and return electrodes, which is about half of the pixel radius (Figure 2A). As a result, the retinal stimulation threshold in such geometry rapidly increases with decreasing pixel size, and it exceeds the charge injection limit for even one of the best electrode materials (SIROF) with pixels below 40 μm in size[8].

One approach to overcoming this problem is based on elevating the return electrode to the top of the inner nuclear layer using a 3-D honeycomb-shaped array, thereby orienting the electric field vertically within the

wells (Figure 2B)[8]. This arrangement decouples the field penetration depth from the pixel width and greatly reduces the stimulation threshold because the vertical field matches the orientation of the bipolar cells in the retina[8]. Although initial animal studies have shown promising results with retinal migration into the subretinal wells, functional activity of the migrated neurons into 3-D arrays remains to be confirmed. In addition, the fabrication process of the honeycomb structures with a local return electrode needs to be further developed.

Here, we present an alternative approach to high-resolution prosthetic vision with a planar monopolar subretinal implant[9], where the high penetration depth and high contrast are enabled by the spatiotemporal modulation of the pixels, utilizing conductivity of the photodiodes under direct bias. Accumulation of charge at the electrode-electrolyte interface and coupling of the electric potentials from the neighboring pixels in the electrolyte elevate the voltage on active electrodes. Since the forward current of the photodiode exponentially increases with the forward voltage, some pixels can reach sufficient conductivity to become transient local returns. Therefore, pre-charging some of the active electrodes makes them effective return electrodes for the next image frame, when these pixels become dark while others are activated. The distance between the active electrode and the neighboring return electrode affects the penetration depth of the electric field into the tissue (Figure 2C). Such pre-conditioning of the pixels to become transient returns in the next image frame enables flexible control of the lateral and axial confinement of electric field in tissue by spatiotemporal modulation of the images projected onto the photovoltaic array. Such an optical current steering strategy allows optimization of the stimulation depth and lateral selectivity for every patient, depending on the retinal thickness and its proximity to the implant[10].

In modeling of such an operation, we first characterize the spatial coupling of electric potential among the pixels using a static finite-element method, and then compute the circuit dynamics of the photovoltaic array, taking into account the inter-pixel coupling, from which the potential in the electrolyte is derived as a function of space and time. The computational results are validated by comparison to ex-vivo measurements of the electric potential in the electrolyte, as well as to electrograms recorded on the corneas of rats implanted with photovoltaic arrays. Most importantly, we demonstrate for the first time that prosthetic acuity in blind rats with subretinal implants composed of 20 μm pixels matches their natural acuity limit of about 28 μm.

Results

Computational modeling of electric field in tissue

The charge accumulated at the electrode-electrolyte interface of a photovoltaic pixel discharges by forward-biased conduction through the diode, driven collectively by the potential at the electrode-electrolyte capacitance due to charge accumulation and the effect of electric potentials from the neighboring pixels. When the forward current through the diode becomes comparable to the stimulation current of the neighboring pixels, such a discharging pixel serves as a transient return. Such a local return electrode limits the spread of electric fields from adjacent pixels, reducing the crosstalk and limiting the field penetration into the tissue (Figure 2C). The cross-pixel impedance between two adjacent electrodes can be defined as $R_{1,2} = {V_{1,2}}/{I_1}$, where I_1 is the current injection of electrode 1, and $V_{1,2}$ is the potential rise at electrode 2 caused by I_1. The finite-element model (COMSOL) of the subretinal photovoltaic array with 40 μm pixels yields $R_{1,2}$ in the range of 15 to 30 kΩ, depending on the location of the electrodes in the array. Each pixel in the hexagonal mesh is surrounded by 6 neighbors, and the stimulation current is typically between 0.1 and 1 μA. Therefore, the spatial coupling of electric potentials in the electrolyte may elevate the electrode potential close to the turn-on voltage of the Si diode (about 0.5 V).

Figure 3 shows the effect of such transient returns on a grating pattern, with every other line of the 40 μm pixels activated by illumination at 1 mW/mm^2. In this calculation, we assumed exact alignment of the light pattern to the pixels. Misalignment will cause some smearing and decrease in contrast, varying over time due to the eye movements. Since the activation function of the bipolar cell stimulation can be closely approximated by a trans-cellular voltage step (between the dendritic to axonal ends)[11], we plot a potential difference between 10 μm above the implant (bottom of the BC dendrites) to 57 μm - the middle of the IPL, where the axonal terminals of the average BC are located[8], as illustrated in Figure 2A. When the electrode-electrolyte interfaces of the dark pixels are biased to 0.5 V prior to the light pulse, the potentials in the electrolyte above the dark pixels drop below 0 V, thereby providing a 100% contrast (Figure 3B,D). On the contrary, if the electrochemical potential bias is much below the turn-on voltage of the diode, for example, 0.2 V, the dark pixels are not conductive and hence do not

transform into transient returns. Therefore, the contrast is reduced below 30% as a result of a strong crosstalk from the neighboring pixels (Figure 3B,C). Contrast decreases even further if the array is composed of smaller pixels, and it also declines with distance from the implant. Such a low contrast precludes high-resolution prosthetic vision in general, and grating acuity measurements, in particular.

Experimental validation of the model

We recorded the electric potential generated by the photovoltaic array in Dulbecco's phosphate-buffered saline (DPBS) under 10 ms NIR (880nm) pulses repeated at 40Hz, using a pipette electrode positioned 20 μm above a pixel in a Petri dish. First, the device was driven to the steady state under uniform full-field illumination at a peak irradiance of 8 mW/mm^2 (Figure 4A). Then a field stop in the projection system was rapidly closed between the two laser pulses, restricting the illumination to an octagonal area of about 1 mm in width, as shown in Figure 4B,C. The electric potential outside the field stop was recorded during the transition into the post-closure steady state. Although the recorded pixel in the shadowed area does not inject current after the closure, positive pulses are still detectable in the post-closure steady state due to crosstalk from the illuminated pixels. However, during the transition period, instead of such a positive pulse, a negative dip was observed at the onset of the first light pulse after the closure (Figure 4D, t=0 ms), demonstrating the crosstalk suppression by the transient returns, as predicted by our model.

To further validate the spatiotemporal model in an implanted rat eye, we calculated the electrical signal generated by the implant at the cornea for various pulse repetition rates, ranging from 1 to 125 Hz with full-field illumination and with alternating gratings. For this purpose, we created a computational model of the rat's eye[12] and a head, with the photovoltaic array implanted in the subretinal space (Figure 5A), as described in detail in Methods and the Supplementary Materials. The modeling results were compared with the in-vivo measurements of the corneal potential relative to a reference electrode in the nose. With a full-field illumination at 1.2 mW/mm^2 of 4 ms in duration repeated at 1 Hz, the amplitude of the corneal potential was in the range of 2 to 3.5 mV, varying between animals and with the position of the electrode on the cornea. As shown in Figure 5B, modeling closely matches the shape of the measured corneal signal. Due to variation of the corneal signals across animals, we normalized the frequency dependence plot by the amplitude at 1 Hz before averaging. As shown in Figure 5C, frequency dependence of the corneal signal also closely matches the model. Amplitude of the visually evoked potentials (VEPs) decreases with increasing frequency much faster than the corneal signals, dropping to the noise level near 60 Hz (flicker fusion). For this reason, we performed the acuity measurements at pulse repetition rate of 64 Hz, as described in the next section.

Grating acuity in natural and prosthetic vision

Measurements of the VEP in response to alternating gratings is a common method of assessing vision in animal models[13] or infants[14]. We recorded VEP via transcranial electrodes above the visual cortices in Royal College of Surgeons (RCS) rats having subretinal photovoltaic implants and in Long Evans (LE) rats, as a normally sighted control. The corneal signal generated by the implant was also recorded for characterization of the implant's current injection. For prosthetic vision, grating images were delivered with NIR light (880 nm) at 1.2 mW/mm^2 peak irradiance at the retina using 4 ms pulses at 64 Hz repetition rate, while the pattern reversal occurred every 500 ms (Supplementary Figure S5). We evaluated the prosthetic visual acuity with implants having 40 μm and 20 μm pixels. For the natural visual acuity measurements, images of the black-and-white gratings presented on a screen under continuous illumination also alternated every 500 ms.

The prosthetic VEP waveforms contained both a 2-Hz signature induced by the grating reversal, and a 64-Hz component of the carrier frequency, including the stimulus artifact. We used the corneal signal as a template to remove the artifact and filtered out the high frequency components. Amplitude of the grating reversal response was measured as the peak-to-peak voltages in the VEP waveform between 0 and 100 ms. The natural grating acuity is typically defined in angular resolution units, i.e. cycles per degree (cpd), and is determined in electrophysiological measurements by the intersection of the logarithmic fitting line with the noise level in a log-linear plot[15,16]. We followed this convention (Figure 6), but to relate the resolution to the pixel size, we plotted the VEP amplitude vs. the inverse bar width (half a cycle). In this conversion, we utilized the fact that one degree of the visual angle corresponds to 64.3 ± 2.9 μm on the retina, as described in Methods. Corresponding plots in the linear units of bar widths are shown in Supplementary Figure S6.

For prosthetic vision with 40 μm implants, the visual acuity was found to be 34.3 ± 5.5 μm, matching the pixel pitch in a hexagonal array p = 40μm·cos (30°) = 34.6 μm. With 20 μm pixels, however, the grating acuity did not match the pixel pitch of 17.3 μm. Instead, it was 27.1 ± 3.8 μm, matching the natural grating acuity of 27.9 ± 2.8 μm, measured in LE rats, as shown in Figure 6.

Discussion

All previous studies with subretinal photovoltaic implants showed that the prosthetic visual acuity matches the pixel pitch (100 μm in humans[5], 75 and 55 μm in rats[17,18]), just as the case with our 40 μm pixels in this study. Here, however, we demonstrated that prosthetic visual acuity with 20 μm pixels is not limited by the pixel pitch, but rather matches the 28 μm natural visual acuity limit in rats, indicating that with such small pixels, resolution appears to be limited by the retinal network integration in rats rather than by the sensor size. However, in humans, where the 20/20 vision corresponds to 5μm stripes on the retina, we hope that 20 μm pixels will enable restoration of central vision in AMD patients with a visual acuity as high as 20/80.

An electric field around the pixels could be optimally confined by adjusting the distance between the active and return electrodes. Such optical configurability of the electric field enables optimization of the field penetration depth for individual patients, tailored to their particular retinal thickness and the implant's proximity to bipolar cells[19]. At the same time, properly restricting the field penetration depth may allow avoiding the direct activation of the tertiary retinal neurons: the amacrine and ganglion cells. Ideally, this could be accomplished if each pixel would have an independent control of its conductivity at any moment of time. This could be done, for example, by including a photosensitive transistor connected in parallel with a primary photodiode in each pixel, which would respond to a wavelength different from the primary NIR light. However, this would greatly complicate the implant design and fabrication. Here we describe a much more practical approach to such field confinement.

The monopolar photovoltaic array, having a common return electrode at the edge of the implant or on its back, allows using some of the active electrodes as anodes and some as cathodes, depending on their pre-charging history and light intensity on each pixel. Due to charge accumulation during previous exposures, the electrode potential stays close to the diode turn-on voltage, so its forward current balances the photocurrent corresponding to the average light intensity. Additional pre-conditioning of the photovoltaic pixels in real time can be based on images captured by the camera. For a typical image refresh rate of 30 Hz, each frame lasts about 33 ms. Photovoltaic stimulation pulses typically range from 0.8 to 10 ms[5], leaving 23 ms for the pre-charging phase preceding the stimulation phase in each frame. Upon image acquisition, the sufficiently dark pixels will be designated to become the local returns and will be exposed to light below the stimulation threshold to accumulate additional charge prior to activation of the bright pixels in the image. Then, during the stimulation phase, the brighter pixels are illuminated with intensity and duration corresponding to the desired charge injection, while the pre-charged dark pixels sink the current injected from the nearby active pixels. This pre-conditioning strategy has the potential to achieve field confinement and hence a high spatial resolution, with a delay not exceeding one frame relative to the image acquisition. To accelerate the image processing for determining which pixels need to be pre-conditioned, predictive tracking algorithms, such as the Kalman filter or exponential smoothing, could be applied. This approach may also allow stretching the pre-charging over several frames.

Another strategy for reducing the cross-talk could be a sequential stimulation spread over the whole 33 ms of the frame duration. With the average pulse duration of about 4ms, only about 4/33 = 12% of the pixels can be activated simultaneously, and even fewer than that, if the images are sparse. In such a distributed activation, pixels become the transient returns after their light is turned off, while other pixels are turned on. With a stimulation spread over the frame duration, however, eye movements may shift the projected image and introduce some uncertainty regarding the relative location of the active and return electrodes. During the slow drift (< 0.25 deg/s), the 2.5 μm/frame image shift is negligible compared to the 20 μm pixel size, but it becomes noticeable during microsaccades, which occur 1-2 times a second[20]. On average, the eye movements velocity is about 1 deg/s[21], corresponding to about 10 μm/frame at 30 Hz frame rate, which imposes a lower limit on pixel size for predictable activation, unless eye tracking is employed or frame rate is increased to reduce this uncertainty.

In conclusion, we demonstrated a prosthetic vision with a resolution matching the natural acuity in rats, using a novel design of a photovoltaic array, where electric field confinement is achieved dynamically, by turning the designated pixels into transient returns. This method enables customized field shaping for each patient and paves the way to prosthetic vision with acuity exceeding 20/100.

Figure Captions

Figure 1. A) Diagram of the cellular layers in healthy retina, including the Choroid (Ch), Retinal Pigmented Epithelium (RPE), Photoreceptors (PR), Horizontal cells (HC), Bipolar cells (BC), Amacrine cells (AC), Inner Plexiform Layer (IPL), and Ganglion cells (GC), who's axons comprise the Nerve Fiber layer (NFL). B) Degenerate retina with a subretinal prosthesis composed of 20 μm wide and 30 μm deep photovoltaic pixels, which convert incoming light into electric current flowing through the tissue and polarizing the nearby neurons.

Figure 2. Electric field above the photovoltaic pixels (40 μm in width) of various geometries. A) A bipolar pixel containing a central active and a circumferential return electrode. (B) A honeycomb-shaped pixel with elevated return electrode. (C) Two monopolar pixels without local returns, where the active electrode of the left pixel acts as an anode and the one on the right – as a cathode, collecting 75% of the anodal current. Remaining current is collected by a global return around the edge of the device. Bottom panels show the corresponding simulated electric fields overlaid on a histology of a degenerate rat retina (current = 68 nA). Diagram of a bipolar cell with its axonal terminals in the middle of IPL in the left panel illustrates its position and size with respect to the field penetration depth. The arrows represent current magnitude on a log scale.

Figure 3. Electric field in electrolyte generated by the grating pattern with and without preconditioning of the dark pixels. A) Photovoltaic array of 1.5 mm in diameter composed of monopolar pixels of 40 μm in width, with a common return electrode (indicated by *) along the edge of the implant. B) Electric potential in electrolyte 10 μm above the implant relative to the middle of IPL (57 μm), plotted along the dash line shown in (A), when the dark pixels are non-conductive (red) and preconditioned (blue). C, D) Magnified view of the electric potential and current in the medium for the two plots in B. Length of the arrows represents the 0.6 power of the magnitude of the current density for visualization.

Figure 4. Near-field electric potential in electrolyte 20 μm above the photovoltaic array. A) View of the array and a pipette electrode under full-field illumination. B) The partially illuminated array after closure of the field stop. The pipette is at the same location, in the shaded zone. C) Map of the electric potential at 0.6 ms. D) Electric potential induced by 10 ms pulses of NIR light before (<0 ms) and after (>0 ms) the decrease of the illuminated area.

Figure 5. Far-field electric potential in the eye: measurements and modeling. (A) Finite element model (FEM) of a rat eye and orbital tissues, with a subretinal photovoltaic implant having 40 μm pixels. Electric potential generated by one electrode injecting 1 μA of current (an elementary field), shown in a color scale optimized for the corneal potential. An inset shows the current density on a logarithmic scale. (B) Measured and modeled corneal potential generated by a 4 ms pulse at 1.2 mW/mm^2 full-field illumination. (C) Peak-to-peak amplitude of the corneal signals induced by 4ms pulses at repetition rates varying from 1 to 125 Hz under full-field illumination. Modeling result is shown by a line.

Figure 6. Prosthetic and natural visual acuity in rats. A) Example VEP waveforms in response to alternating gratings in RCS rats with implants and in LE rats. B-D) VEP amplitude as a function of the grating density (in units of the inverse bar width, 1/μm) for prosthetic vision with 20 μm pixels (B), 40 μm pixels (C), and natural vision (D).

Methods

Modeling and ex-vivo validation of the implant performance

We modeled the electric field in the retina generated by a subretinal 30μm-thick array 1.5 mm in diameter with 40-μm photovoltaic pixels, described in detail in[9]. In this array, each pixel has a SIROF-coated active electrode 18 μm in diameter exposed to electrolyte. The return electrodes are connected to a SIROF-coated common return deposited at the periphery of the implant, as shown in Figure 3A. The electric field at any given time is a linear combination of a set of elementary fields, each of which corresponds to activation of one pixel individually, with coefficients equal to the currents at the respective active electrodes[19]. We generated the elementary electric fields of all pixels by numerically solving the Poisson equation of volume conduction, using the finite element method (FEM) in COMSOL Multiphysics 5.6 (COMSOL, Inc., Sweden), the model file of which is accessible online[22]. The boundary condition on the capacitive electrode-electrolyte interface of a SIROF electrode

change from equipotential (EP) to a uniform current density (UCD)[23], with a time constant of t≈RC, which is 0.24 ms for the active electrodes, and 40 ms for the return electrode. Since the pulse width in our measurements ranges from 4 ms to 10 ms, we assumed the UCD boundary condition for the active electrodes and EP - for the return.

To model the spatial coupling of the electric potential between pixels, we generalized the access resistance of one electrode to the cross-resistance matrix **R** of all active electrodes, where the entry in row *i* and column *j* corresponds to the potential elevation at an active electrode *i*, caused by a unitary current injection from an active electrode *j* [19]. The diagonal entries of **R** represent the access resistance of each active electrode. To compute the interrelated circuit dynamics of all pixels, we then generalized the equation of the nonlinear circuit dynamics of a photovoltaic pixel[24] to the multi-dimensional form, as shown in Supplementary Materials. The multi-dimensional nonlinear differential equation was solved with our customized adaptive-step gradient descent method in MATLAB R2017a (MathWorks, MA), the source code of which is accessible online[25]. To compute the electric field in the retina, the elementary electric fields were linearly combined using coefficients obtained from the multi-dimensional circuit dynamics.

For validation of the spatiotemporal model, we placed the device in a Petri dish filled with Dulbecco's phosphate-buffered saline (DPBS). The 10-ms pulses of 880-nm laser light were projected on the device surface at a repetition rate of 40 Hz at intensity of 8 mW/mm^2. Micropipettes with a 5μm tip diameter were used to measure the electric potential 20 μm above the device. To study the current dynamic under changing images, a field stop in the laser projection system swiftly closed between two laser pulses, reducing the illuminated area from full-field to an octagon covering about a quarter of the pixels (Figure 4A). Electric potential before and after the closure was modeled and compared to the measurement.

Modeling the corneal signals and the in-vivo validation

To model the electric potential generated by a subretinal implant on the cornea, we constructed an anatomically realistic model of the rat eye, as described by Selner *et al.* [12], with adaptation for the thickness of a degenerate retina and a photovoltaic implant in the subretinal space. The corresponding COMSOL model file is accessible online[22]. We also incorporated a realistic geometry of the rat head to the model and computed the potential difference between the corneal and the nasal electrodes, as shown in Figure S4A in Supplementary Materials. Meshing and adjusting the complex geometry of the rat head was difficult and computationally slow, and since the initial result demonstrated that electric potential is confined to a few millimeters around the eye, we approximated the head geometry with a cylinder, while keeping all the ocular and orbital tissues the same as in the anatomically accurate model. This approximation resulted in a similar electric field, but with a more reliable meshing and adjustable geometry. Electric potential generated by a single activated pixel in such a simplified layout is shown In Figure 5A, overlaid with the diagram of the ocular anatomy. A more detailed diagram of the anatomical structures and the list of the tissue properties with the corresponding references are shown in the Supplementary Materials.

Surgical procedures

All experimental procedures were conducted in accordance with the Statement for the Use of Animals in Ophthalmic and Vision research of the Association for Research in Vision and Ophthalmology (ARVO) and approved by the Stanford Administrative Panel on Laboratory Animal Care. Royal College of Surgeons (RCS) rats were used as an animal model of the inherited retinal degeneration, and Long Evans (LE) rats were used as a control group with healthy natural vision. Animals are maintained at the Stanford Animal Facility under 12h light/12h dark cycles with food and water ad libitum.

The planar photovoltaic devices were implanted in the subretinal space, as previously described[26], typically at 6 months of age, after a complete loss of the outer nuclear layer, as evidenced by optical coherence tomography (OCT; HRA2-Spectralis; Heidelberg Engineering, Heidelberg, Germany). The implants were placed in the temporal-dorsal region, approximately 1 mm away from the optic nerve. A total of 9 animals were implanted with 1.5 mm diameter arrays containing pixels of 40 μm (n=4) and 20 μm (n=5). Animals were anesthetized with a mixture of ketamine (75 mg/kg) and xylazine (5 mg/kg) injected intraperitoneally.

To visualize the retina and the implant, animals were monitored over time using OCT. For measurements of the visually evoked potentials (VEP), each animal was implanted with three transcranial screw electrodes: one

electrode over each hemisphere of the visual cortex (4 mm lateral from midline, 6 mm caudal to bregma), and a reference electrode (2 mm right of midline and 2 mm anterior to bregma).

Measurements of the prosthetic visual acuity

Following anesthesia and pupil dilation, the cornea was covered with a viscoelastic gel and a cover slip to cancel the cornea optical power and ensure good retinal visibility. The retinal implant was illuminated with a customized projection system, consisting of an 880 nm laser (MF-880 nm-400 μm, DILAS, Tucson, AZ), customized optics, and a digital micromirror display (DMD; DLP Light Commander; LOGIC PD, Carlsbad, CA) for pattern projection. The entire optical system was integrated with a slit lamp (Zeiss SL-120; Carl Zeiss, Thornwood, NY) for real-time observation of the illuminated retina via a CCD camera (acA1300-60gmNIR; Basler, Ahrensburg, Germany).

Visual acuity was assessed by applying alternating gratings, where the NIR illumination was pulsed at 64 Hz and the grating patterns were switched at 1 Hz. The grating bar width ranged from 13 μm to 157 μm on the retina while the light intensity was set to 1.2 mW/mm^2. The light intensity was measured before and after each measurement at the cornea and scaled by the ocular magnification squared, where magnification is defined as the ratio between the size of a projected square on the retina and in air. VEPs were recorded using the Espion E3 system (Diagnosys LLC, Lowell, MA) at a sampling rate of 2 kHz and averaged over 250 trials. Corneal signal reflecting the device performance was simultaneously measured using ERG electrodes, relative to the reference electrode in the nose. The corneal signal was also used as a template to remove the device artifact in VEP waveforms. High frequency components in VEP traces were further filtered using a spectrum reconstruction method. Acuity was defined as an intersection of the logarithmic fitting line with the noise level.

Measurements of the natural visual acuity

For measurements of the natural acuity under visible light, we could not utilize the same system used for prosthetic vision because the latter was optimized for NIR light and exhibited strong chromatic aberrations at visible wavelengths, resulting in a significant loss of contrast in fine patterns. Therefore, we measured monocular natural acuity in LE rats (n=5) with a conventional large white screen in angular units (cycle per degree), and then related it to the linear resolution (μm) on the retina.

Following anesthesia, the cornea was covered with a plano contact lens and animals were placed 23 cm away from a 40 cm-wide white screen, providing luminance of 51 cd/m^2 on the cornea. Black-and-white rectangular-wave grating patterns of 50% duty cycle alternated at 1 Hz, providing 500 ms exposure duration for each pattern. Stripe widths varied from 0.21 to 16.7 mm on the screen, corresponding to 9.6 to 0.12 cycles per degree (cpd) in the eye. VEP measurements were averaged over 100-150 cycles.

To relate the angular units of acuity (cpd) to the stripe width on the retina (μm), we performed spot retinal photocoagulation (PASCAL laser, Topcon, San Jose, CA). Animals were anesthetized and mounted on a gonioscopic stage, and retinal laser burns were produced for 3 angular positions separated by 4 degrees each. The 577 nm wavelength laser with a spot diameter of 100 μm was centered on the pupil for each exposure of 70 ms in duration at 70 mW of power (or two sequential pulses of 100ms at 50 mW). Retinal burns were then imaged together with the NIR grating pattern projected into the eye in our slit-lamp based VEP system used for the measurements of prosthetic acuity, as described above. Distance between the centers of the burns was measured using the NIR patterns as a scale bar. The resulting conversion factor was found to be 64.3 ± 2.9 μm per degree of the visual angle, very similar to the 65.3 ± 6.7 μm/deg based on optical modeling of the rat eye[27]. The uncertainty range in this conversion is represented by horizontal error bars in Figure 6D. Logarithmic line was fit to the falling trend of the plot, excluding the edge data point corresponding to the maximum value. Acuity was defined as a crossing point of the fitting line with the noise floor.

Acknowledgements

Studies were supported by the National Institutes of Health (Grants R01-EY-027786 and P30-EY-026877), the Department of Defense (Grant W81XWH-19-1-0738), AFOSR (Grant FA9550-19-1-0402), Wu Tsai Institute of Neurosciences at Stanford, and unrestricted grant from Research to Prevent Blindness. Photovoltaic arrays were fabricated at the Stanford Nano Shared Facilities (SNSF) and Stanford Nanofabrication Facility (SNF), which are supported by the National Science Foundation award ECCS1542152. K.M. was supported by a Royal Academy of

Engineering Chair in Emerging Technology, UK. We would like to thank Dr. Tong Ling for his help with the design and assembly of the optical system for prosthetic acuity measurements and its software.

Author contributions statement

B. Wang conducted the electrophysiological measurements, Z.C. Chen performed the computational modeling and ex-vivo characterization of the implant, M. Bhuckory performed the implantations and in-vivo imaging and helped with prosthetic acuity measurements, T. Huang, A. Shin and L. Galambos worked on fabrication of the implants under the guidance of T. Kamins and K. Mathieson. V. Zuckerman conducted natural acuity measurements and helped with prosthetic acuity measurements, E. Ho built the system and helped with the software development for natural acuity measurements. Ethan Rosenfeld worked on the computational model of the eye and head in COMSOL. D. Palanker guided the research and data analysis. All authors participated in writing the manuscript.

Additional information

D. P. and T. K. serve as consultants to Pixium Vision. D. P.'s patents related to retinal prostheses are owned by Stanford University and licensed to Pixium Vision. All other authors declare no financial interests.

References

1. Wong, W.L., *et al.* Global prevalence of age-related macular degeneration and disease burden projection for 2020 and 2040: a systematic review and meta-analysis. *Lancet Glob Health* **2**, E106-E116 (2014).
2. Liew, G., Michaelides, M. & Bunce, C. A comparison of the causes of blindness certifications in England and Wales in working age adults (16-64 years), 1999-2000 with 2009-2010. *Bmj Open* **4**(2014).
3. Kim, S.Y., *et al.* Morphometric analysis of the macula in eyes with geographic atrophy due to age-related macular degeneration. *Retina* **22**, 464-470 (2002).
4. Humayun, M.S., *et al.* Morphometric analysis of the extramacular retina from postmortem eyes with retinitis pigmentosa. *Invest Ophth Vis Sci* **40**, 143-148 (1999).
5. Palanker, D., Le Mer, Y., Mohand-Said, S., Muqit, M. & Sahel, J.A. Photovoltaic Restoration of Central Vision in Atrophic Age-Related Macular Degeneration. *Ophthalmology* **127**, 1097-1104 (2020).
6. Edwards, T.L., *et al.* Assessment of the Electronic Retinal Implant Alpha AMS in Restoring Vision to Blind Patients with End-Stage Retinitis Pigmentosa. *Ophthalmology* **125**, 432-443 (2018).
7. Loudin, J.D., *et al.* Optoelectronic retinal prosthesis: system design and performance. *Journal of Neural Engineering* **4**, S72-S84 (2007).
8. Flores, T., *et al.* Honeycomb-shaped electro-neural interface enables cellular-scale pixels in subretinal prosthesis. *Sci Rep* **9**, 10657 (2019).
9. Huang, T.W., *et al.* Vertical-junction photodiodes for smaller pixels in retinal prostheses. *J Neural Eng* (2021).
10. Chen, Z.C., Wang, B.Y. & Palanker, D. Real-Time Optimization of the Current Steering for Visual Prosthesis. in *2021 10th International IEEE/EMBS Conference on Neural Engineering (NER)* 592-596 (2021).
11. Werginz, P., Wang, B.-Y., Chen, Z.C. & Palanker, D. On optimal coupling of the 'electronic photoreceptors' into the degenerate retina. *Journal of Neural Engineering* **17**, 045008 (2020).
12. Selner, A.N., Derafshi, Z., Kunzer, B.E. & Hetling, J.R. Three-Dimensional Model of Electroretinogram Field Potentials in the Rat Eye. *IEEE Trans Biomed Eng* **65**, 2781-2789 (2018).

13. Harnois, C., Bodis-Wollner, I. & Onofrj, M. The effect of contrast and spatial frequency on the visual evoked potential of the hooded rat. *Exp Brain Res* **57**, 1-8 (1984).
14. Hamilton, R.*, et al.* VEP estimation of visual acuity: a systematic review. *Documenta ophthalmologica. Advances in ophthalmology* **142**, 25-74 (2021).
15. Boyes, W.K. & Dyer, R.S. Pattern reversal visual evoked potentials in awake rats. *Brain Res Bull* **10**, 817-823 (1983).
16. Kharauzov, A.K.*, et al.* Objective measurement of human visual acuity by visual evoked potentials. *Neurosci Behav Physiol* **36**, 1021-1030 (2006).
17. Lorach, H.*, et al.* Photovoltaic restoration of sight with high visual acuity. *Nature Medicine* **21**, 476-482 (2015).
18. Ho, E.*, et al.* Characteristics of prosthetic vision in rats with subretinal flat and pillar electrode arrays. *J Neural Eng* **16**, 066027 (2019).
19. Chen, Z.C., Wang, B. & Palanker, D. Real-Time Optimization of the Current Steering for Visual Prosthesis. in *IEEE EMBS NER'21* (2021).
20. Alexander, R.G., Macknik, S.L. & Martinez-Conde, S. Microsaccade Characteristics in Neurological and Ophthalmic Disease. *Front Neurol* **9**, 144 (2018).
21. Ko, H.K., Snodderly, D.M. & Poletti, M. Eye movements between saccades: Measuring ocular drift and tremor. *Vision Res* **122**, 93-104 (2016).
22. Chen, Z.C. COMSOL models for the paper "Electronic "photoreceptors" enable prosthetic vision with acuity matching the natural resolution in rats". 5081278 (Zenodo.org, 2021).
23. Chen, Z., Ryzhik, L. & Palanker, D. Current Distribution on Capacitive Electrode-Electrolyte Interfaces. *Physical Review Applied* **13**, 014004 (2020).
24. Boinagrov, D.*, et al.* Photovoltaic Pixels for Neural Stimulation: Circuit Models and Performance. *IEEE Trans Biomed Circuits Syst* **10**, 85-97 (2016).
25. Chen, Z.C. CCCharlesChan/RP_multidim_circuit_solver: Retinal Prosthesis Multi-Dim Circuit Solver v1.0. 5081286 (Zenodo.org, 2021).
26. Lorach, H.*, et al.* Performance of photovoltaic arrays in-vivo and characteristics of prosthetic vision in animals with retinal degeneration. *Vision Res* **111**, 142-148 (2015).
27. Lozano, D.C. & Twa, M.D. Development of a rat schematic eye from in vivo biometry and the correction of lateral magnification in SD-OCT imaging. *Invest Ophthalmol Vis Sci* **54**, 6446-6455 (2013).

Figure 1

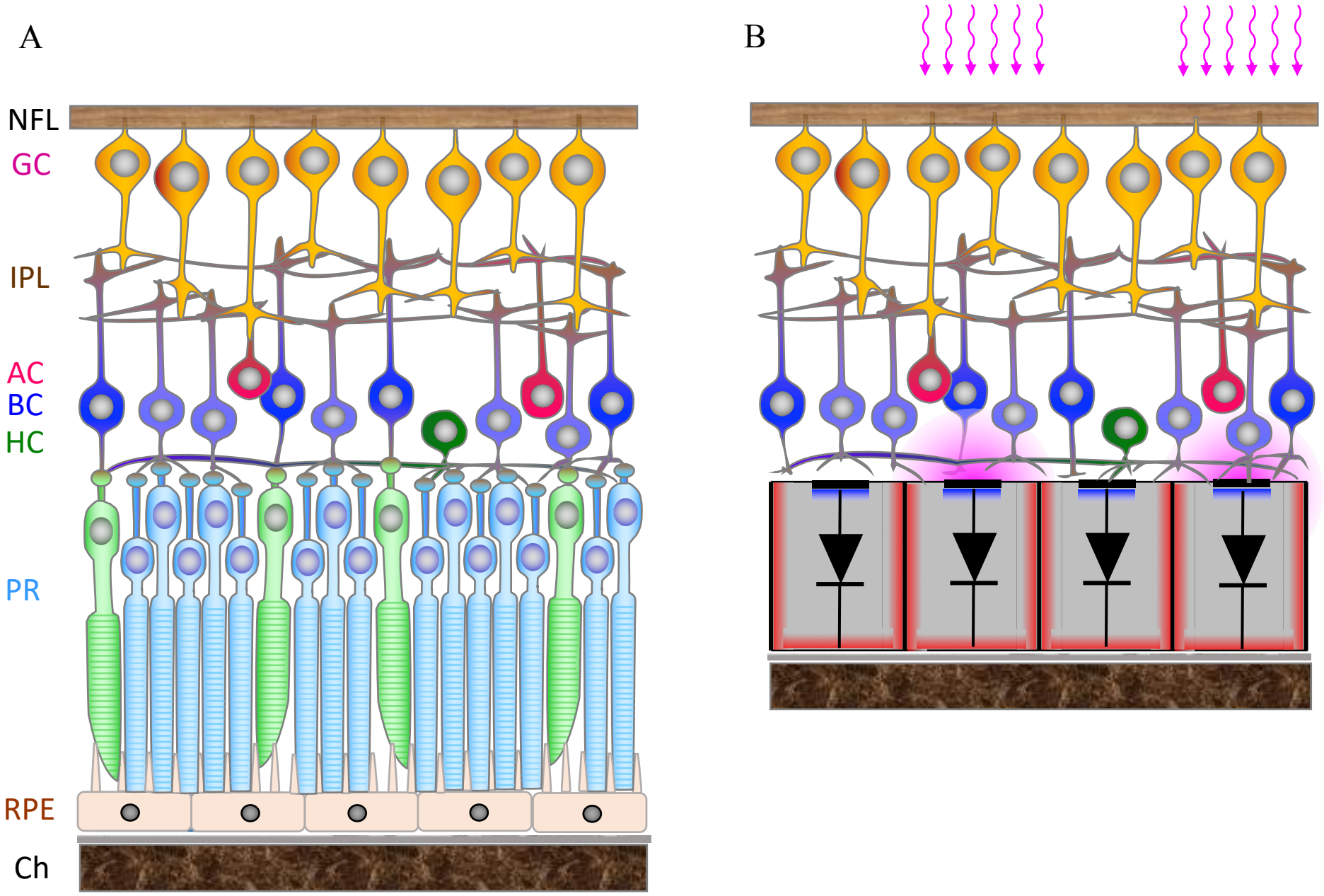

Figure 2

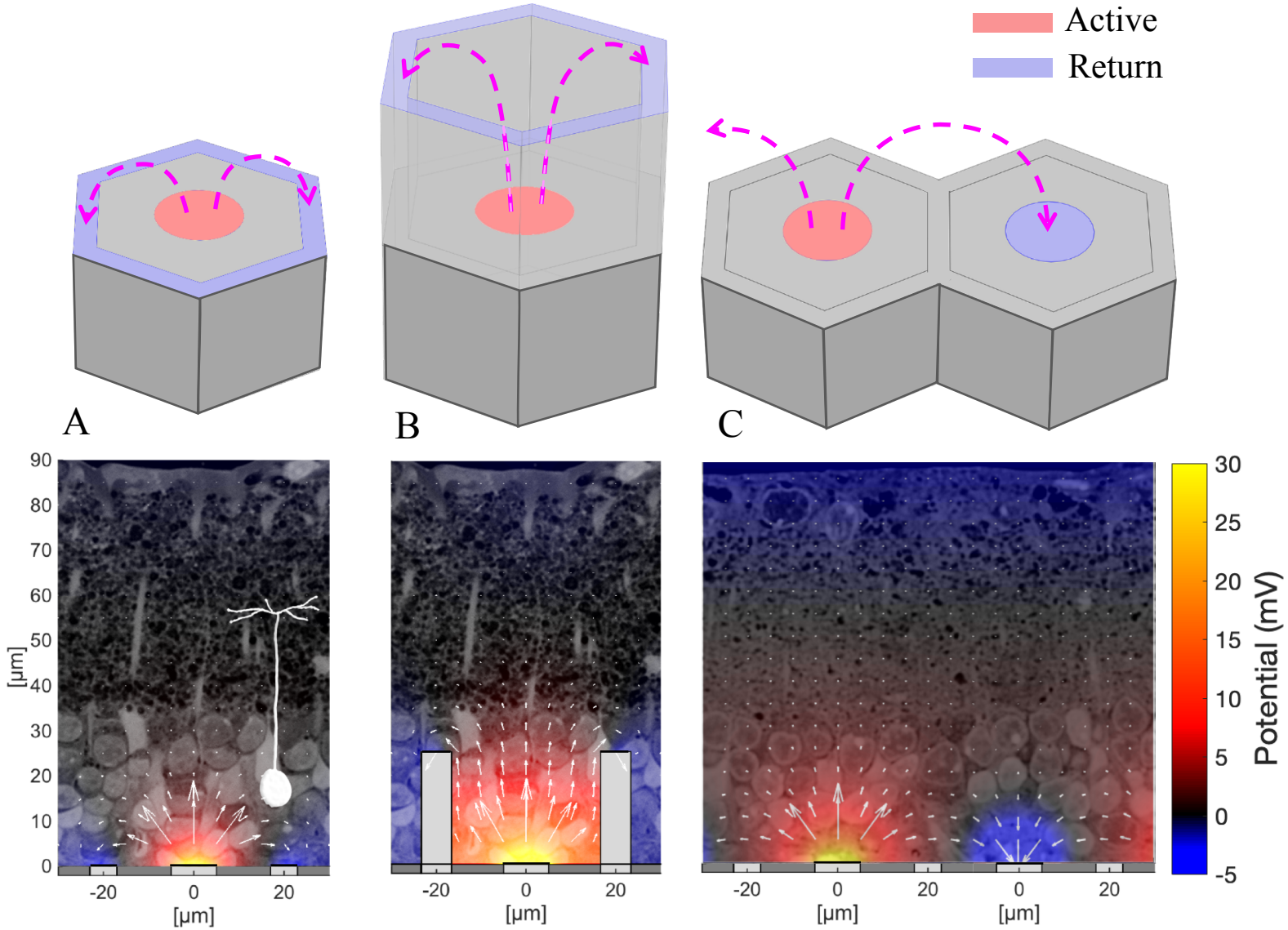
Active
Return
A
B
C
90
80
70
60
50
40
30
20
10
0
[µm]
-20
0
20
[µm]
30
25
20
15
10
5
0
-5
Potential (mV)

Figure 3

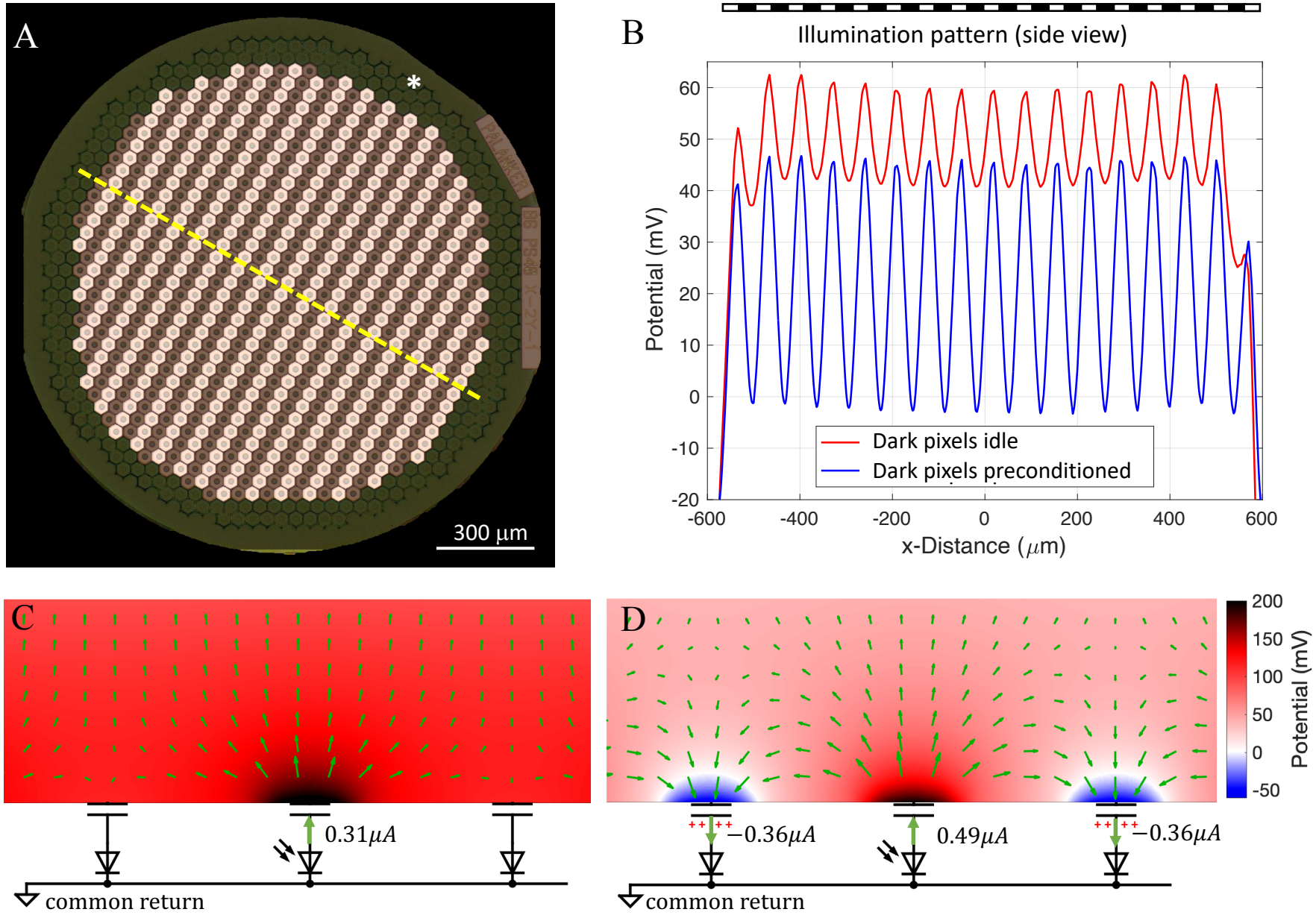
A
300 µm
B
Illumination pattern (side view)
Potential (mV)
x-Distance (µm)
Dark pixels idle
Dark pixels preconditioned
C
0.31µA
common return
D
−0.36µA
0.49µA
−0.36µA
common return
Potential (mV)

Figure 4

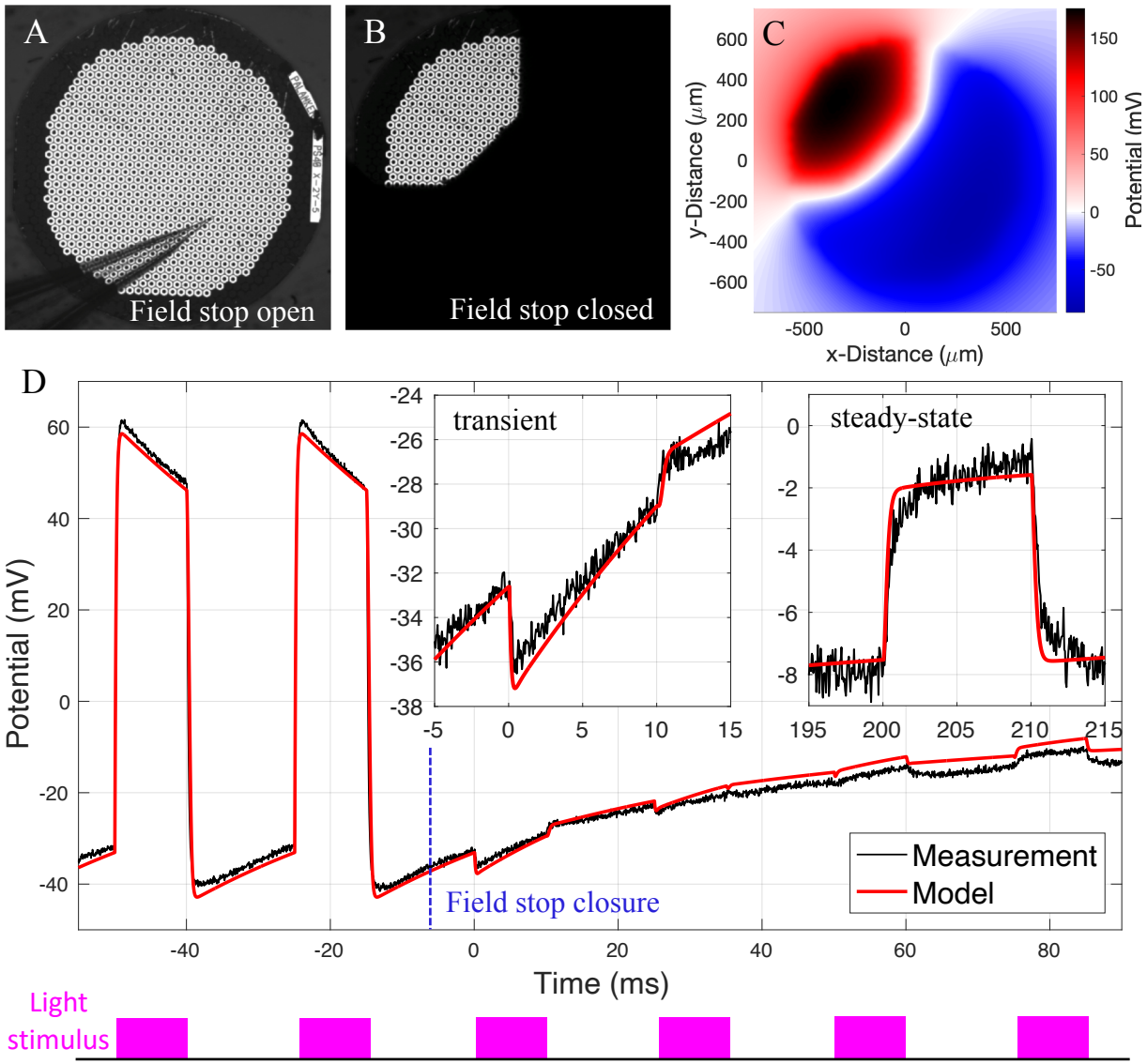
A
Field stop open
B
Field stop closed
C
y-Distance (μm)
x-Distance (μm)
Potential (mV)
D
Potential (mV)
transient
steady-state
Field stop closure
Measurement
Model
Time (ms)
Light stimulus

Figure 5

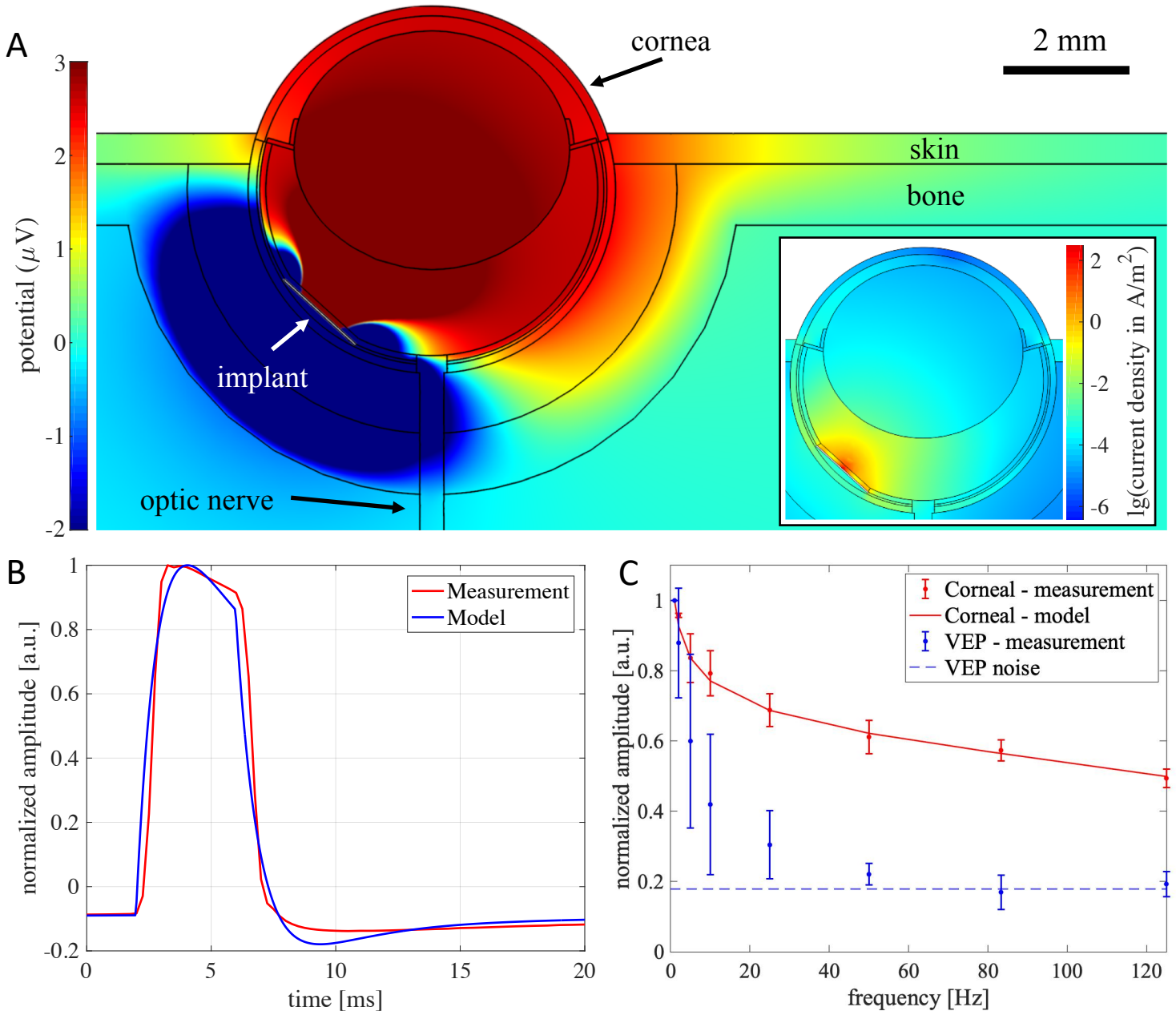
A
cornea
2 mm
skin
bone
implant
optic nerve
potential (μV)
3
2
1
0
-1
-2
lg(current density in A/m²)
2
0
-2
-4
-6
B
Measurement
Model
normalized amplitude [a.u.]
time [ms]
C
Corneal - measurement
Corneal - model
VEP - measurement
VEP noise
normalized amplitude [a.u.]
frequency [Hz]

Figure 6

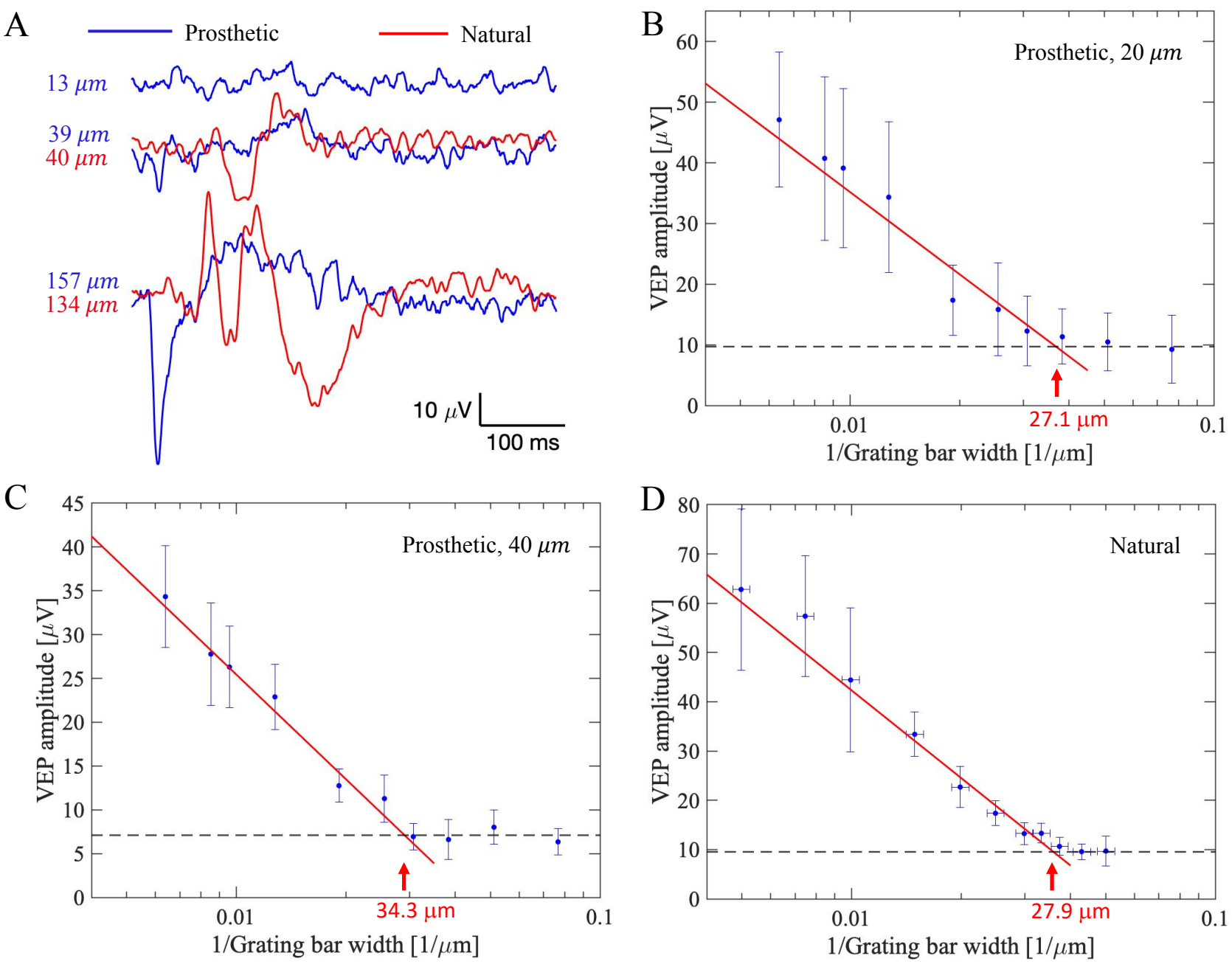
A
Prosthetic
Natural
13 μm
39 μm
40 μm
157 μm
134 μm
10 μV
100 ms
B
Prosthetic, 20 μm
VEP amplitude [μV]
1/Grating bar width [1/μm]
27.1 μm
C
Prosthetic, 40 μm
VEP amplitude [μV]
1/Grating bar width [1/μm]
34.3 μm
D
Natural
VEP amplitude [μV]
1/Grating bar width [1/μm]
27.9 μm